Effect of Fe segregation on the migration of a non-symmetric Σ5 tilt grain boundary in Al

M.I. Mendelev[a] and D.J. Srolovitz[b]
Princeton Materials Institute & Department of Mechanical & Aerospace Engineering, Princeton University, Princeton, New Jersey 08544

G.J. Ackland
Department of Physics and Astronomy, University of Edinburgh, Edinburgh EH9 3JZ, Scotland, United Kingdom

S. Han
Department of Physics, Ewha Womans University, Seoul 120-750, Korea

(Received 16 June 2004; accepted 18 October 2004)

We present an analysis, based upon atomistic simulation data, of the effect of Fe impurities on grain boundary migration in Al. The first step is the development of a new interatomic potential for Fe in Al. This potential provides an accurate description of Al–Fe liquid diffraction data and the bulk diffusivity of Fe in Al. We use this potential to determine the physical parameters in the Cahn–Lücke–Stüwe (CLS) model for the effect of impurities on grain boundary mobility. These include the heat of segregation of Fe to grain boundaries in Al and the diffusivity of Fe in Al. Using the simulation-parameterized CLS model, we predict the grain boundary mobility in Al in the presence of Fe as a function of temperature and Fe concentration. The order of magnitude and the trends in the mobility from the simulations are in agreement with existing experimental results.

I. INTRODUCTION

All models for microstructural evolution require information on how the underlying defects move. For example, in grain growth and recrystallization, the key piece of information is the mobility of the grain boundaries. While there have been a very large number of studies of grain growth and recrystallization, there have been very few studies that directly focused upon the measurement of grain boundary mobility (e.g., Ref. 1 or 2). Studies focusing on the mobilities of grain boundaries include several experimental (for review, see Ref. 3) and simulation investigations (e.g., Refs. 4 and 5). Until recently, it was impossible to make a direct comparison between the computer simulation and experimental results, since most of the reliable experimental data were obtained for Al, Pb and Zn, while the computer simulations were performed using a Lennard–Jones interatomic potential[4,6] and an embedded-atom method (EAM) potential for Ni.[5] While a simulation study of grain boundary migration in Al was performed,[7] direct comparisons with experiment are questionable since the EAM potential used does not accurately reproduce the high temperature properties of Al. In a recent work,[8] we developed a new EAM potential for Al which accurately describes many properties of Al at $T = 0$ [including the face-centered-cubic (fcc) to hexagonal close-packed (hcp) phase transformation energy] and properties associated with melting (the melting temperature, latent heat, change in density upon melting, liquid density). We then used this potential in a molecular dynamics (MD) simulation of the migration of an asymmetric Σ5 tilt grain boundary in pure Al. We found that the temperature dependence of the grain boundary mobility is satisfactorily described by the Arrhenius relation with an activation energy of ~0.3 eV/atom. However, experimental measurements[3] suggest that the activation energy for the reduced mobility is ~0.6 eV/atom in Al for a grain boundary with the same misorientation as that considered in the simulation. The most likely source for the disagreement between simulation and experiment is the presence of impurities in the real material.[8] For example, the purest Al samples used in Ref. 3 had a bulk concentration of impurities of $C_\infty = 0.5$ ppm. An analysis of the

[a]Address all correspondence to this author.
e-mail: mendelev@ameslab.gov
[b]This author was an editor of this journal during the review and decision stage. For the *JMR* policy on review and publication of manuscripts authored by editors, please refer to http://www.mrs.org/publications/jmr.html.
DOI: 10.1557/JMR.2005.0024

experimental data suggests that the heat of segregation in this system is $E_0 = -0.7$ eV/atom.[9] A common estimate of the impurity concentration on the boundary C_0 is

$$C_0 = C_\infty e^{-E_0/kT} \quad . \tag{1}$$

At $T = 450$ °C, this equation implies that $C_0 = 0.04$. In contrast with the bulk impurity concentration, the impurity concentration on the boundary is too large to neglect.

Recall that in a pure system, grain boundary migration requires no net mass transport. However, in an impure system, the grain boundary can drag along its cloud of segregated impurities. This requires net mass transport. As a result, a larger driving force is required to move the boundary at the same velocity (as when no impurities are present). This, in turn, implies that the mobility of a boundary in an impure system can be substantially lower and the activation energy for migration substantially larger than in a pure system. Cahn[10] and Lücke and Stüwe[11] proposed a now classical model for the impurity drag effect (CLS model). While this theory rests on several important oversimplifications (see Ref. 12 for detailed discussion), better analytical models provide only minor improvement. The CLS model suggests that there are two regimes of the grain boundary motion in an impure system: a low-velocity regime, where the boundary mobility is much lower (several orders of magnitude) than that in a pure system and a high velocity regime, where the impurity drag is relatively small. The regime of practical interest is nearly always that for low velocity. If we define the grain boundary mobility as

$$M = \left(\frac{\partial V}{\partial P}\right)_{P=0} \quad , \tag{2}$$

where P is the driving force and V is the steady-state grain boundary velocity, the CLS model predicts[12]

$$M = \frac{1}{1/M^0 + 1/M^{\text{imp}}} \quad , \tag{3a}$$

where M^0 is the grain boundary mobility in the pure system,

$$M^{\text{imp}} = \frac{D}{2n\delta}\frac{1}{C_\infty(1-C_\infty)}\frac{E_0}{(kT)^2}\left[\sinh\left(\frac{E_0}{kT}\right) - \frac{E_0}{kT}\right]^{-1} \quad , \tag{3b}$$

D is the impurity diffusivity, n is the site density on the boundary, and δ is the grain boundary thickness. Thus, to make any estimates using the CLS model, we must determine the grain boundary mobility in the pure system, the heat of segregation and the impurity diffusivity. The grain boundary mobility in pure Al was determined in Ref. 8. In this work, we focus on the heat of segregation. While a real system always contains impurities of several different types (e.g., see Ref. 9), we focus here on only Fe impurities. This choice is based on two reasons. The first is that Fe was found to be a constituent of the high purity Al used in Refs. 9 and 13. The second is that Fe has a very small solubility in Al. This implies that if the Fe concentration is too small to precipitate Al–Fe particles, the Fe should segregate to grain boundaries. Indirect confirmation of this fact was found in Ref. 14.

This paper is organized as follows. First, we develop a semi-empirical potential for Al–Fe alloys. Then we apply this potential to the determination of the distribution of the heat of segregation on the migrating, asymmetric Σ5 tilt grain boundary in pure Al studied in Ref. 8. Finally, using these data, we estimate the concentration of Fe on the grain boundary and the effect of Fe on grain boundary mobility in Al.

II. SEMI-EMPIRICAL POTENTIAL FOR Al–Fe ALLOYS

The total potential energy in the embedded atom method framework[15] has contributions from pairwise and local density terms

$$U = \sum_{i=1}^{N-1}\sum_{j=i+1}^{N}\varphi(r_{ij}) + \sum_{i=1}^{N}\Phi(\rho_i) \quad , \tag{4}$$

where the subscripts i and j label distinct atoms, N is the number of atoms in the system, $r_{i,j}$ is the separation between atoms i and j

$$\rho_i = \sum_j \psi(r_{ij}) \quad , \tag{5}$$

and Φ, φ, and ψ are functions that have yet to be specified.

In the original extension of the EAM method to multicomponent alloys,[16] the functions $\varphi(r)$ depend on the element type of atoms i and j, $\psi(r)$ depends on the element type of atom j, and $\Phi(\rho)$ depends on the element type of atom i. In other words, Eqs. (4) and (5) can be rewritten as

$$U = \sum_{i=1}^{N-1}\sum_{j=i+1}^{N}\varphi^{t_i t_j}(r_{ij}) + \sum_{i=1}^{N}\Phi^{t_i}(\rho_i) \quad , \tag{6}$$

$$\rho_i = \sum_j \psi^{t_j}(r_{ij}) \quad , \tag{7a}$$

where $t_{i(j)}$ is the elemenl type of atom i(j). Thus, an EAM potential for a two-component alloy contains 7 functions (φ^{11}, φ^{12}, φ^{22}, ψ^{11}, ψ^{22}, Φ^1, and Φ^2). Another approach was proposed in Ref. [17]. The authors of this work extended the Finnis–Sinclair (FS) approach[18] to the case of binary alloys. In this extension, both functions φ and ψ depend on the types of atoms i and j. Therefore, Eq. (6)

is still valid in this approach and Eq. (7a) should be replaced with

$$\rho_i = \sum_j \psi^{t_i t_j}(r_{ij}) \quad . \tag{7b}$$

This approach is based on the fact that in the tight binding model, which underlies the Finnis–Sinclair derivation of the potentials, the function ψ^{12} represents the square of the hopping integral. Therefore, this function was chosen as[17]

$$\psi^{12} = \sqrt{\psi^{11}\psi^{22}} \quad . \tag{8}$$

Actually, there is no direct relation between the hopping integral for an alloy and those for the pure elements; thus this function can be adjusted in the fitting. In the case of Al–Fe, refitting the cross potential is particularly reasonable since the hopping represents *s-d* overlap, which is absent in the pure materials.

The EAM potentials for pure Al and pure Fe used in the present study were developed in Refs. 8 and 19. To simulate Fe impurities in Al, we must also develop the cross-functions φ^{AlFe} and ψ^{AlFe}. We did this in the following manner. As a 0th order approximation, we used

$$\varphi^{(0)AlFe} = \frac{\varphi^{AlAl} + \varphi^{FeFe}}{2}; \quad \psi^{(0)AlFe} = \sqrt{\psi^{AlAl}\psi^{FeFe}} \quad . \tag{9}$$

We used the resultant potential to simulate a 128 atom liquid, containing equal numbers of Al and Fe atoms at 1820 K using molecular dynamics. We stopped the simulation after 0.1 ns and import the atomic configuration into a first-principles code (details can be found in Ref. 8) to determine the force on each atom.

Since we are interested only in Al-rich alloys (we examine Fe as an impurity in Al), we also considered two different Al-rich Al–Fe compounds in the fitting procedure. Instead of considering the very complex, stable Al_3Fe phase, we focused on the much simpler DO_3 and $L1_2$ Al_3Fe structures. The FeAl interatomic compound calculations were performed using spin-dependent GGAs and a 20 × 20 × 20 k-point mesh. In practice, the $FeAl_3$ and dilute solutions had zero magnetic moment. There is an error associated with generalized gradient approximation magnetism in Fe_3Al, but it is small compared with the accuracy of the fitting, in which it is assigned low weight on account of our primary interest is in dilute solutions of Fe in Al. The lattice parameters and formation energies of these phases were obtained from first-principles calculations (see Table I). We used these data, together with the first principles forces obtained for the liquid, to refit the φ^{AlFe} and ψ^{AlFe}.

Next, we use the new potential to determine the magnitude of the interaction between a vacancy and a substitutional Fe impurity and compare the result with the same quantity obtained from first-principles calculations.

TABLE I. Data used in fitting the Al-Fe cross-potential.

Property	First principles calculations	New potential
a (Al_3Fe $L1_2$) (Å)	3.7856	3.7855
ΔE^f (Al_3Fe $L1_2$) (eV/atom)[a]	–0.111	–0.103
a (Al_3Fe DO_3) (Å)	5.9692	5.9689
ΔE^f (Al_3Fe DO_3) (eV/atom)[a]	0.002	–0.004
$\Delta E^{v\text{-}1Fe}$ (eV)	0.03	0.04

[a]The formation energy $\Delta E^f(Al_3Fe)$ is defined as the heat of the following reaction: 3/4Al + 1/4Fe = Al_3Fe.

The vacancy–substitutional Fe interaction energy is defined as

$$\Delta E^{V\text{-}S} = E[1,1] - E[0,1] + E[0,0] - E[1,0] \quad , \tag{10}$$

where $E[x,y]$ is the energy of a system of a system containing N fcc lattice sites, where x are occupied by Fe atoms, y by vacancies, and N-x-y by Al atoms (the energy is minimized with respect to atomic displacements and the Fe atoms and vacancies are nearest neighbors in the 1,1 configuration). This quantity is the change in the energy of the system when an Fe atom, initially infinitely far from the vacancy, is exchanged with an Al atom that is a nearest neighbor of the vacancy. For sufficiently large N, $\Delta E^{v\text{-}s}$ does not depend on N. $\Delta E^{v\text{-}s}$ is included in the fitting procedure to account for the interaction of an Fe atom with a region of low density (note such regions are common at a grain boundary).

Using the first principles value of $\Delta E^{v\text{-}s}$, together with the forces in the liquid configuration and the compound properties, we refitted the function φ^{AlFe}, while keeping ψ^{AlFe} fixed. Since $\Delta E^{v\text{-}s}$ is calculated based upon relaxed atomic configurations, its value, calculated with the new interatomic potential, will not be in perfect agreement with the first principles results. Therefore, the entire fitting procedure was iterated to convergence.

The properties of the new Al-Fe system obtained with the new potential are shown in Table I along with the corresponding first principles data. The parameters describing the new potential are presented in Appendix I. Figure 1 shows the pairwise, density, and embedding energy functions of the new potential, along with the effective pair potential

$$\varphi_{eff}^{t_1t_2}(r) = \varphi^{t_1t_2}(r) + \left(\left.\frac{\partial \Phi^{t_1}}{\partial \rho}\right|_{\rho_0^{t_1}} + \left.\frac{\partial \Phi^{t_2}}{\partial \rho}\right|_{\rho_0^{t_2}} \right) \psi^{t_1t_2}(r) \quad , \tag{11}$$

where the superscripts refer to the atom type and ρ_0^t is the value of ρ for atoms of type t in the equilibrium $L1_2$ Al_3Fe compound at $T = 0$.

To test this new potential, we measured the total structure factor of an $Al_{60}Fe_{40}$ liquid alloy (obtained using MD) at $T = 1820$ K. Figure 2 shows that there is very

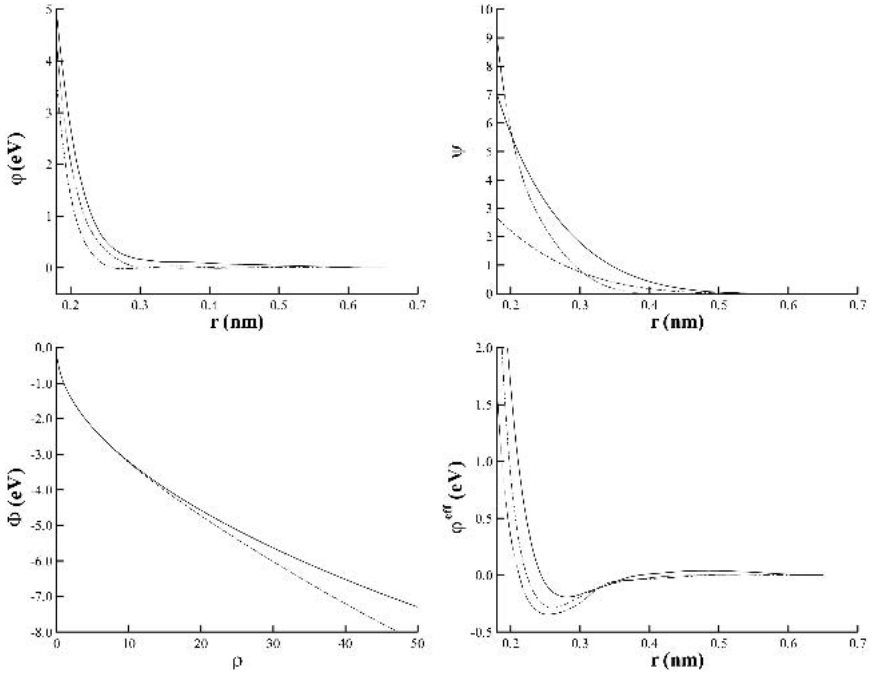

FIG. 1. Semi-empirical potential functions for Al–Fe alloys. Solid, dotted and dash-dotted lines represent Al–Al, Fe–Fe, and Al–Fe pairs.

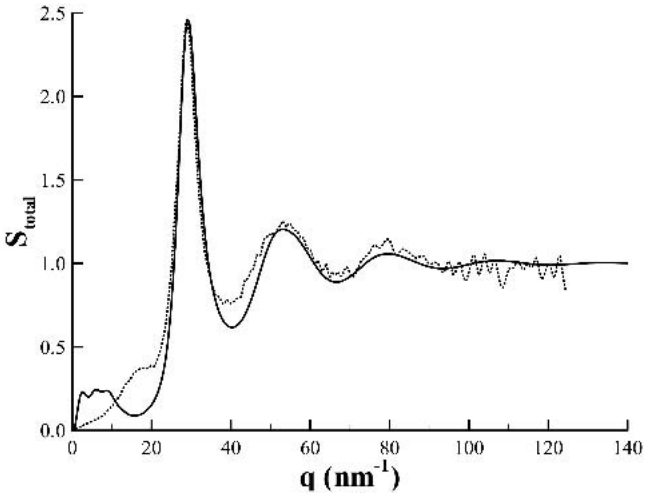

FIG. 2. X-ray total structure factor for $Al_{60}Fe_{40}$ liquid at $T = 1820$ K. The solid and dotted lines represent the simulation and experimental[20] data, respectively.

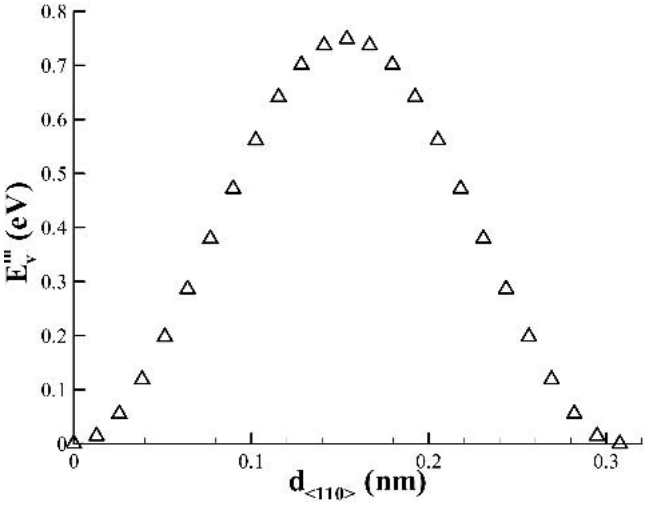

FIG. 3. The energy of a vacancy as it moves along a path in the ⟨110⟩-direction from one stable location to a position currently occupied by an Fe atom in Al, obtained with the new potential. The vacancy migration energy is the maximum value in this plot.

good agreement between the total structure factor obtained from simulation and x-ray diffraction data.[20]

As a second test of the potential, we calculated the activation energy for Fe diffusion in Al. The vacancy formation energy in pure Al was determined using first principles results in Ref. 8. Since the potential for pure Al was fitted to this value, it is accurately reproduced by the potential. The vacancy migration energy was determined by calculating the energy of the crystal as an Fe atom is translated from its initial, equilibrium position into an empty nearest neighbor site (i.e., a vacancy) along a path drawn from the initial equilibrium position to its final equilibrium position (the system is relaxed at each step along this path). The energy versus displacement is shown in Fig. 3; the difference between the maximum and minimum in this plot is the vacancy migration energy, i.e., 0.75 eV. In the vacancy mechanism for self-diffusion, the activation energy is the sum of the relaxed vacancy formation and vacancy migration energies. Using the new Al–Fe potential, we find the activation energy for diffusion of Fe in Al to be 1.44 eV. This result is in excellent agreement with the value of 1.4 eV extracted from Mössbauer spectroscopy data.[21] On the

other hand, the Fe diffusivity obtained from tracer diffusion experiments shows considerable variation, i.e., 1.99 eV[22] or 2.29 eV,[23] and the agreement with the simulation data is less good. The disagreement between the tracer and Mössbauer data, was explained[21] by the formation of stable Fe_4Al_{13} clusters which led to the trapping of Fe atoms in the tracer diffusion experiments. We will explore this question via computer simulation elsewhere.[24]

III. HEAT OF SEGREGATION

There are at least two approaches to examining impurity segregation to a grain boundary. The first is through the determination of the segregation isotherm using Monte Carlo methods (e.g., see Ref. 25). The heat of segregation can be determined by applying this approach over a range of temperatures. The alternative approach is to obtain the heat of segregation by comparing the energies of relaxed bicrystals with an impurity in the bulk and on the grain boundary. The latter approach can be used to determine the distribution of heats of segregation in the grain boundary (rather than an average heat of segregation) and is, therefore, more directly applicable to the CLS model, as described in the following section.

Since the difference in atomic radii of Al and Fe is less than 10%, we assume that the Fe is a substitutial impurity in Al. In this case, we can define the heat of the segregation as the change in energy associated with the exchange of one Al atom from the boundary with one Fe atom from the bulk (including local relaxations). The next methodological question is how to obtain an appropriate grain boundary structure at $T = 0$ K. One approach is to bring two single crystals (with the appropriate relative orientations) into contact and minimize the energy with respect to the atomic coordinates. Several objections could be raised: (i) such a procedure will not necessarily lead to the global minimum of energy and (ii) the boundary structure corresponding to this state (i.e., the global energy minimum structure at $T = 0$) is not necessarily representative of the structure of a grain boundary moving at a high temperature. Therefore, we used an alternative approach. First, we created a bicrystal containing 12179 atoms as described in Ref. 8. The simulation cell size was approximately 40 × 40 × 123 Å (the long direction z is perpendicular to the nominal boundary plane). Since Al is elastically anisotropic, application of a strain to the bicrystal can cause the boundary to migrate. We applied a biaxial strain in the plane of the boundary to drive the migration of the boundary (in the z-direction), as described in Ref. 8. During the course of the MD simulation ($T = 800$ K), the boundary migrated approximately 20 Å, ending in the middle of the simulation cell. Following the removal of the applied strain, the temperature of the boundary was stepwise reduced to 0 K (i.e., the system was held at 800, 700, 500, and 300 K for 0.1 ns followed by static relaxation) under isobaric conditions. We used this $T = 0$ boundary structure in our determination of the distribution of the heats of segregation. There were 963 Al atoms located within ±5 Å of the mean boundary position. We sequentially replaced each of these Al atoms with an Fe atom, relaxed the structure, and determined the energy of the system. To obtain the heat of segregation, we subtracted the energy of the bicrystal with an Fe atom replacing one of the Al atoms far from the grain boundary. Figure 4 shows the distribution of the heats of segregation. Only 36.8% sites have a negative heat of segregation and are, therefore, favorable for segregation.

With this information in hand, we are prepared to estimate the coefficient of segregation. Recall that the segregation isotherm assumed in the CLS model (at zero velocity) is the Langmuir isotherm

$$C_0 = \frac{C_\infty e^{-E_0/kT}}{1 - C_\infty + C_\infty e^{-E_0/kT}} \quad , \tag{12}$$

which accounts for the effects of site saturation not included in the original CLS model. However, in this equation, the grain boundary is assumed to be homogeneous. Figure 4 demonstrates that the heat of segregation can take on different values at different locations within the grain boundary; hence, this assumption is invalid.

If we assume that segregation at each boundary site occurs independently from all of the other boundary sites, we can rewrite Eq. (11) as

$$C_0 = \frac{1}{N_s} \sum_{i=1}^{N_s} \frac{C_\infty e^{-E_{0i}/kT}}{1 - C_\infty + C_\infty e^{-E_{0i}/kT}} \quad , \tag{13}$$

where E_{0i} is the heat of segregation associated with site i and N_s is the total number of boundary sites. Of course,

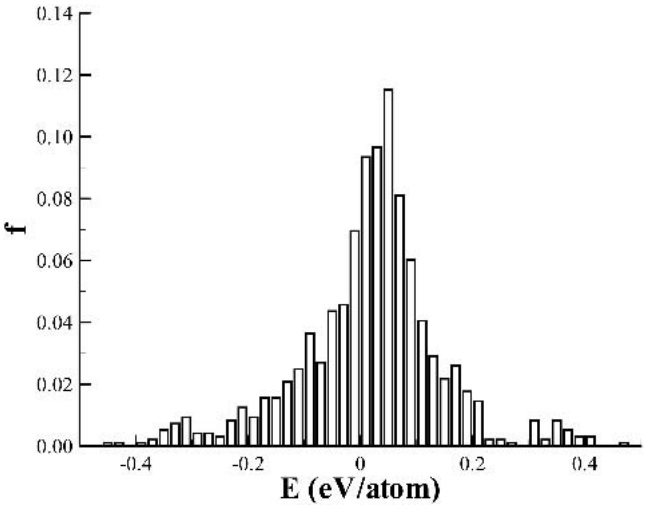

FIG. 4. The distribution of the heat of segregation to sites within ±δ/2 of the grain boundary.

this approximation is reasonable only if the deviation from ideality is either negative (or at least not very large and positive) and the impurity concentration on the boundary is so small that impurity atoms are not too near one another. Using the new potential, we find that the heat of solution of Fe in fcc Al at $T = 0$ is –0.20 eV/atom in the dilute limit. This heat of solution is the difference in energy between a large fcc Al crystal with and without one iron atom minus the energy per atom of pure body-centered-cubic (bcc) Fe. Since this quantity is negative, we expect the deviation from ideality is negative. In the present study, we consider cases in which the impurity concentration on the boundary does not exceed 1% such that the second condition for the validity of Eq. (13) is satisfied.

Figure 5 shows the segregation isotherms at $T = 600$ K (the lowest temperature used in the simulation of grain boundary migration in[8]) and $T = 400$ K calculated using Eq. (13). At $T = 600$ K the isotherm is almost linear and at $T = 400$ K it is slightly sublinear. Even at $T = 400$ K, the Fe concentration on the boundary is much smaller than 1% (although it is more than 1000 times larger than the bulk concentration). We can define the segregation coefficient as

$$s = C_0/C_\infty \quad . \tag{14}$$

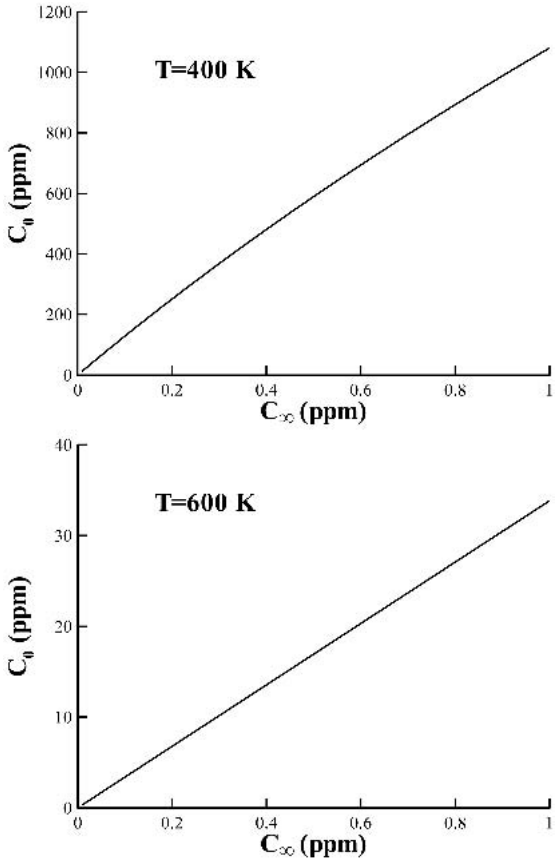

FIG. 5. Average Fe concentration with the boundary layer versus the bulk concentration of Fe.

The average heat of segregation can be defined as

$$\Delta H_{seg} = -RT^2 \frac{d \ln s}{dT} \quad . \tag{15}$$

Figure 6 shows the logarithm of the segregation coefficient versus inverse temperature. Since this curve is slightly superlinear, the average heat of segregation appears to decrease with increasing temperature. This effect can be understood as follows. At a low temperature, the impurities sit only at the sites with large heats of segregation. As the temperature is increased, the impurities increasingly occupy sites with lower heats of segregation such that the average heat of segregation is lower. Overall, the average heat of segregation changes from –0.40 eV/atom at 400 K to –0.28 eV/atom at 850 K with a mean value of –0.36 eV/atom over this entire temperature range.

Equation (13) gives the average impurity concentration in a boundary layer of thickness δ. This quantity gives us an idea of how the boundary layer is enriched by the impurities but it is ambiguous in the sense that it depends on the value of δ. A more rigorous approach is to use the Gibbs definition of the adsorption (i.e., the Gibbsian excess)

$$\Gamma = n \int_{-\infty}^{\infty} (C - C_\infty) dz \quad . \tag{16}$$

If C differs from C_∞, only over some distance δ of the grain boundary, we can rewrite this equation as

$$\Gamma = n \frac{\delta}{N_s} \sum_{i=1}^{N_s} (C_{0i} - C_\infty) \quad , \tag{17}$$

where N_s is the number of atomic sites in the layer of

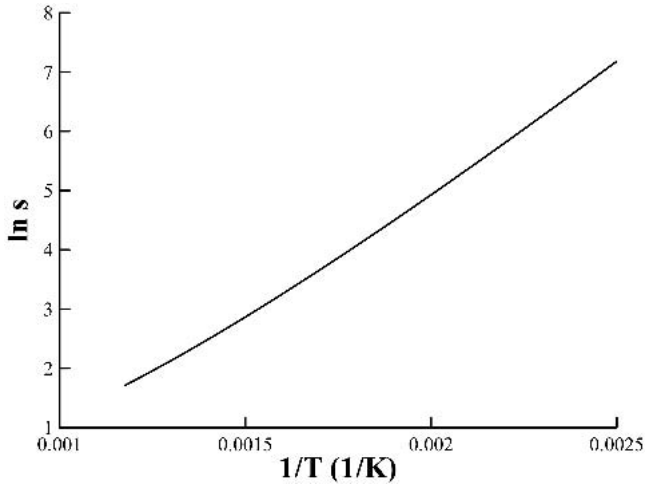

FIG. 6. Temperature dependence of the segregation coefficient s.

thickness δ (i.e., for δ sufficiently large, Γ does not depend on the choice of δ). Using C_{0i} from Eq. (11), we finally obtain

$$\Gamma = C_\infty(1 - C_\infty)n \frac{\delta}{N_s} \sum_{i=1}^{N_s} \frac{e^{-E_{0i}/kT} - 1}{1 + C_\infty(e^{-E_{0i}/kT} - 1)} \quad . \tag{18}$$

Figure 7(a) shows the Gibbsian excess as a function of the bulk impurity concentration (segregation isotherm) at two temperatures, calculated using Eq. (17). The temperature dependence of Γ is shown in Fig. 7(b). These plots are reminiscent of Figs. 5 and 6.

IV. IMPURITY DRAG

While the CLS model was derived assuming that the grain boundary is a homogeneous layer, our simulations demonstrate that it is not. Therefore, the CLS model should be extended to describe the observed heterogeneity. Since our goal here is to estimate the magnitude of the impurity drag effect, we use a simplified approach. First, we note that according to the CLS model, the average drag force on a grain boundary from an impurity located within the boundary layer of thickness δ is

$$P_{hom}^{imp} = 2 \frac{V}{D} C_\infty(1 - C_\infty) \frac{(kT)^2}{E_{0i}} \left[\sinh\left(\frac{E_{0i}}{kT}\right) - \frac{E_{0i}}{kT} \right] \quad .$$

Therefore, in the case of a heterogeneous boundary, the drag force per unit area of boundary is

$$P_{het}^{imp} = 2 \frac{1}{A} \frac{V}{D} C_\infty(1 - C_\infty) \sum_{i=1}^{N} \frac{(kT)^2}{E_{0i}} \left[\sinh\left(\frac{E_{0i}}{kT}\right) - \frac{E_{0i}}{kT} \right] \quad ,$$

where N is the total number of atoms in the system. Of course, P_{het}^{imp} does not depend on N since E_{0i} is nonzero only for atoms near the grain boundary. Replacing A in terms of N_s and δ, as above, we can rewrite the drag force as

$$P_{het}^{imp} = 2n \frac{\delta}{N_s} \frac{V}{D} C_\infty(1 - C_\infty) \sum_{i=1}^{N} \frac{(kT)^2}{E_{0i}} \left[\sinh\left(\frac{E_{0i}}{kT}\right) - \frac{E_{0i}}{kT} \right] \quad .$$

Since $M = V/P$, we finally obtain

$$\frac{1}{M^{imp}} = \frac{2n}{D} C_\infty(1 - C_\infty) \frac{\delta}{N_s} \sum_{i=1}^{N_s} \frac{(kT)^2}{E_{0i}} \left[\sinh\left(\frac{E_{0i}}{kT}\right) - \frac{E_{0i}}{kT} \right] \quad . \tag{19}$$

If we associate the diffusivity in Eq. (15) with the Fe bulk diffusivity in Al reported in Ref. 21, $D = 1.2 \times 10^{-5} e^{-1.4\text{eV}/kT}$ m^2/s, we can evaluate the dependence of the grain boundary mobility on Fe concentration (Fig. 8). This plot shows that impurity drag is important if the impurity concentration is greater than 0.01 ppm at $T = 850$ K and greater than 1 ppb at $T = 600$ K. While we believe that these concentrations, where impurity drag is important, may be underestimates (see the next section), these estimates demonstrate that the impurity drag effect cannot be a priori neglected even in the purest real materials. The observation that the mobility is independent

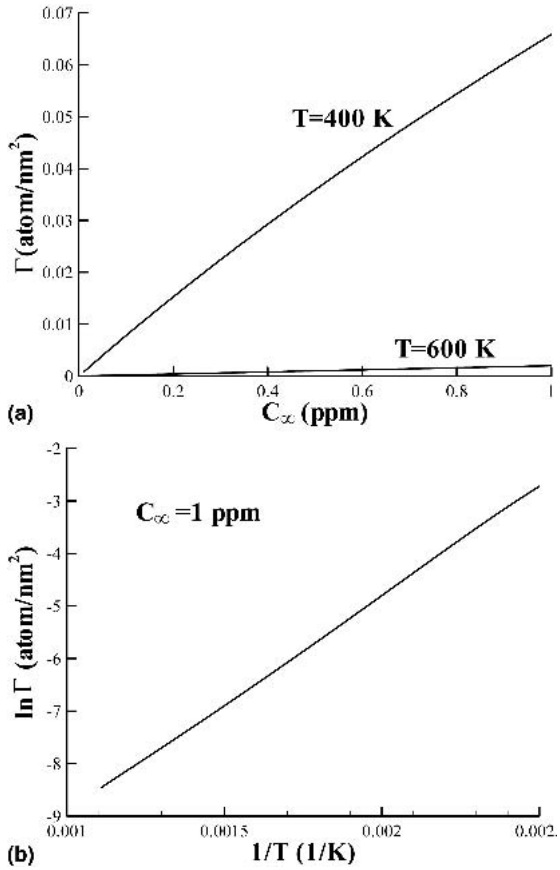

FIG. 7. Gibbsian excess of Fe versus (a) Fe bulk concentration and (b) inverse temperature.

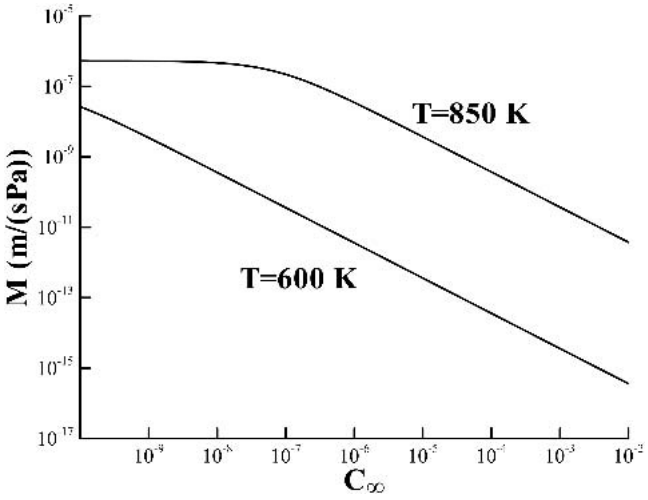

FIG. 8. The Σ5 ⟨100⟩ tilt grain boundary mobility as function of Fe bulk concentration. This calculation does not account for the limited Fe solubility in Al.

of impurity concentration for $C_\infty < 0.1$ ppm at $T = 850$ K simply reflect the fact that the impurity drag effect is very small under these conditions such that that the overall mobility is dominated by the intrinsic drag [see Eq. (3a)]. We note that the mobility associated with impurity drag M_i decreases much more quickly with decreasing temperature than does the intrinsic boundary mobility M_0. Therefore, the overall mobility becomes nearly impurity concentration independent at a smaller impurity concentration at low temperature.

Figure 9 shows the temperature dependence of the grain boundary mobility in Arrhenius coordinates. The $C_\infty = 0$ curve is linear with a slope simply equal to the activation energy for grain boundary mobility in the pure system. For $C_\infty = 1$ ppm, the curve is also linear, but in this case, the slope is determined solely by the impurity drag effect. The curves for intermediate concentrations are not linear; the high temperature slope is close to that for the pure system while the low temperature slope is dictated by the impurity drag effect. The activation energies shown in Fig. 10 were calculated at high temperature. This plot demonstrates that the activation energy for grain boundary migration is nearly impurity concentration independent below 1 ppb and above 10 ppm. Figure 10 also shows the experimentally determined activation energies for the reduced mobilities of a Σ5 ⟨100⟩ (the same misorientation as considered in the present study) and a non-special ⟨100⟩ tilt grain boundaries.[3] In these cases, C_∞ is the total concentration of all types of impurities which are present in the sample. These experimental data also show that the activation energy depends on the impurity concentration only over a relatively small region of concentration in Fig. 10. The experimental and simulation activation energy versus impurity concentration results show very similar forms except for a rigid shift. The simulation-parameterized CLS theory consistently shows that the impurity drag effect is important at bulk impurity concentrations that is significantly smaller than that seen in experiment.

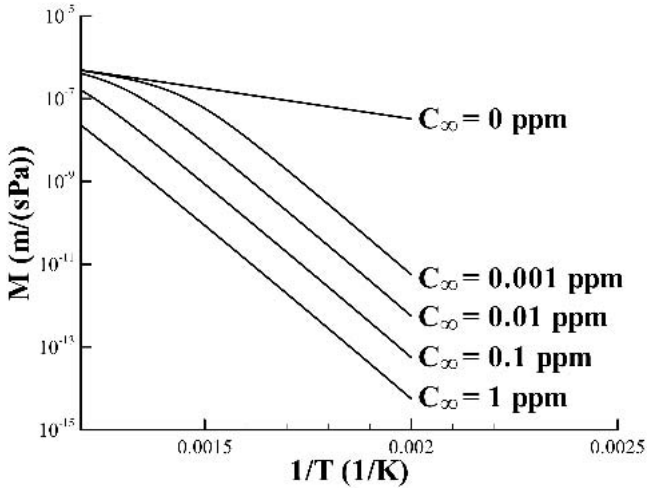

FIG. 9. The temperature dependence of the Σ5 ⟨100⟩ tilt grain boundary mobility in Al in the presence of Fe impurities.

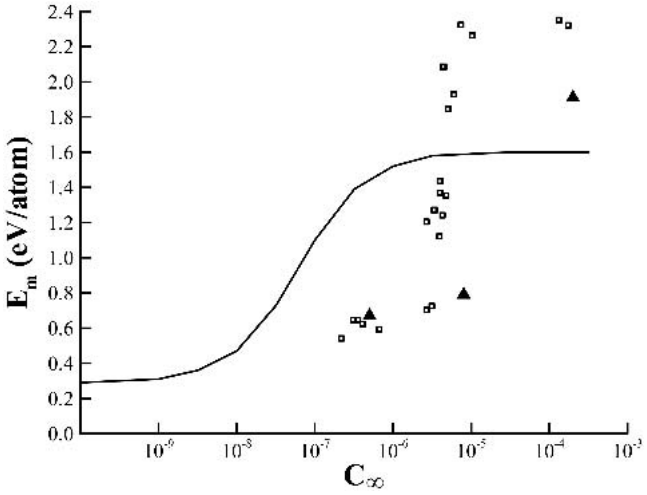

FIG. 10. The dependence of the activation energy for the migration of a Σ5 ⟨100⟩ tilt grain boundary in Al in the presence of Fe impurities obtained from the simulation and CLS model (solid line). The squares and triangles represent the experimental data for the reduced mobilities of a Σ5 ⟨100⟩ and a non-special ⟨100⟩ tilt grain boundaries.[3] The calculation does not account for the limited Fe solubility in Al.

V. DISCUSSION

We developed a new, semi-empirical interatomic potential for Al–Fe alloys (this work and Ref. 8). The potentials were fitted to both bulk properties of Al obtained from experiment and first-principles calculations of bulk and defect properties for Al, Fe, and a series of Al–Fe compounds. We demonstrated that this potential yields a good description of the structure of liquid Al–Fe alloys and the diffusivity of Fe in Al (these data were not used in the fitting procedure). We used this potential in a series of MD simulations designed to determine the mobility of one particular grain boundary in pure Al. To determine the effect of Fe impurities on grain boundary mobility, we determined the heat of segregation of Fe to the same grain boundary and used it within the CLS model for impurity drag. This represents the first application of the CLS model for impurity drag where all of the input parameters were independently determined from simulation.

Unfortunately, it is difficult to make a direct comparison between the simulation-parameterized CLS model prediction and the experimental data. The first difficulty is associated with the fact that the experiments were based upon curvature driven boundary migration, from which it is only possible to obtain the reduced mobility A (i.e., the product of the mobility and the grain boundary stiffness $\gamma + \gamma''$)

$$A = M(\gamma + \gamma'') \quad , \tag{20}$$

where γ is the boundary free energy and γ'' is its second derivative with respect to boundary inclination. While there are some data for γ, no data are available for γ'' for any grain boundary. Since the experiments were performed using curved boundaries, the reduced mobility data represent an average over a range of grain boundary inclinations. Another difficulty in comparing the boundary mobility obtained from simulation with experiment is that simulations and experiments consider physically different systems. Simulations tend to focus on pure materials, while truly pure materials do not exist. This inability to make such comparisons is particularly problematic since it is the boundary mobility in pure Al that is our most reliable prediction because it is obtained directly from atomistic simulation (without reliance on any theory). Although the mobility of boundaries in pure Al is not, in itself, important for the CLS model under most realistic conditions, such a comparison could verify the quality of the new interatomic potential for defects in Al. However, the heat of segregation of Fe to grain boundaries in Al also depends on the grain boundary structure and, therefore, on the quality of the potential. Finally, although the present study of the effects of impurities on boundary migration focuses on the role of Fe impurities in Al, even the purest experimental samples contain a variety of different impurities.

Because of these difficulties in making a quantitative comparison of the simulation-parameterized CLS prediction with experiment, we can only check whether our calculations predict the same order of magnitude of the grain boundary mobility measured in experiments. To make such a comparison, we estimate the boundary stiffness as $\gamma + \gamma'' \sim 0.5$ J/m^2 and explicitly assume that all of the impurities in the material create the same drag as does Fe. A comparison of the simulation results with the experimental data is shown in Fig. 11. This comparison shows that the simulation-parameterized CLS model yields the same order of magnitude of the mobility as seen in experiment. However, the simulation results performed with an Fe concentration of 8 ppm leads to an overestimate of the activation energy for the mobility. This is consistent with the data shown in Fig. 10. This figure also shows the onset of significant drag begins at lower impurity concentrations in the simulations than in experiment. This can be traced to one or more of the following issues: the CLS model is oversimplified (see Ref. 12), some of the impurities may be less potent than Fe in causing drag, and/or the assumption that the Fe diffusivity in the CLS model is its bulk diffusivity in Al. The last issue may be the most important if the segregated impurities diffuse along with the moving boundary. In such a case, the appropriate impurity diffusivity may be closer to that of its diffusivity in the grain boundary (low activation energy) rather than in the bulk. On other hand, Fig. 10 demonstrates that at large impurity concentrations the experimental activation energies for migration are even larger than those predicted in our calculations. This may be associated with the formation of very small Al–Fe compound particles (or clusters) at the grain boundary if the local impurity concentration is sufficiently large. Such an effect cannot be described within the ideal solution framework of the CLS model.

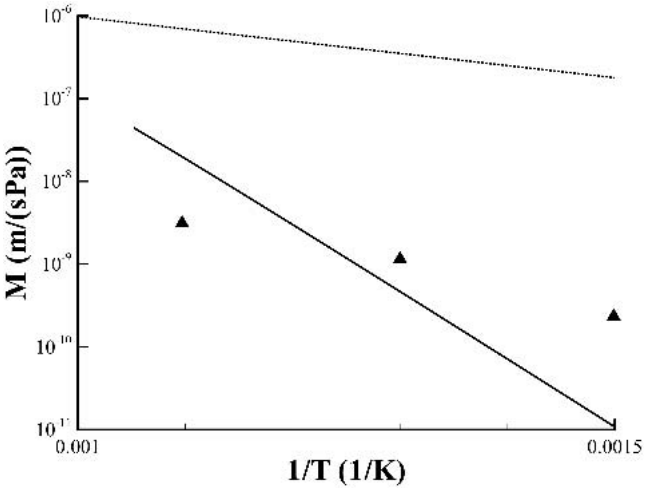

FIG. 11. The temperature dependence of the Σ5 ⟨100⟩ tilt grain boundary mobility. The solid and dotted lines are the simulation results for $C_\infty = 8$ ppm and $C_\infty = 0$ ppm,[8] respectively. The triangles are extracted from the experimental results for the reduced mobility for the same boundary in Al when the total impurity concentration is $C_\infty = 8$ ppm.[13]

ACKNOWLEDGMENTS

M.I.M. and D.J.S. thank Prof. B.S. Bokstein, Prof. G. Gottstein, Prof. L.S. Shvindlerman, and Prof. D.A. Molodov for useful discussions. This research was supported by the United States Department of Energy, Office of Basic Energy Sciences, through Grant No. DE-FG02-99ER45797 with Princeton University and the Computational Materials Science Network.

REFERENCES

1. *Grain Growth in Polycrystalline Materials II*, edited by H. Yoshinaga, T. Watanabe, and N. Takahashi (Transtec, Zurich, Switzerland, 1996).
2. *Interface Science*, **10** (2002).
3. G. Gottstein and L.S. Shvindlerman: *Grain Boundary Migration in Metals: Thermodynamics, Kinetics, Applications* (CRC Press, Boca Raton, FL, 1999).
4. B. Schonfelder, D. Wolf, S.R. Phillpot, and M. Furtkamp: Molecular-dynamics method for the simulation of grain-boundary migration. *Interface Sci.* **5,** 245 (1997).
5. H. Zhang, M.I. Mendelev, and D.J. Srolovitz: Computer simulation of the elastically-driven migration of a flat grain boundary. *Acta Mater.* **52,** 2569 (2004).
6. M. Upmanyu, R.W. Smith, and D.J. Srolovitz: Vacancy generation during grain boundary migration. *Interface Sci.* **6,** 41 (1998).
7. H. Zhang, M. Upmanyu, and D.J. Srolovitz: Curvature driven

grain boundary migration in aluminum: Molecular dynamics simulations, *Acta Mater.* (in press).
8. M.I. Mendelev, D.J. Srolovitz, G.J. Ackland, S. Han, and J.R. Morris: Atomistic simulation of grain boundary migration in Al. (unpublished).
9. D.A. Molodov, U. Czubayko, G. Gottstein, and L.S. Shvindlerman: On the effect of purity and orientation on grain boundary motion. *Acta Mater.* **46,** 553 (1998).
10. J.W. Cahn: Impurity-drag effect in grain boundary motion. *Acta Metall.* **10,** 789 (1962).
11. K. Lucke and H.P. Stuwe: On the theory of grain boundary motion, in *Recovery and Recrystallization of Metals,* edited by L. Himmel, (Interscience, New York, 1963), p. 171.
12. M.I. Mendelev and D.J. Srolovitz: Impurity effects on grain boundary migration. *MSMSE* **10,** R79 (2002).
13. L.S. Shvindlerman and E.M. Fridman: Mobility of Incline Boundaries in Aluminum, Fizika Tverdogo Tela **15** (12), pp. 3700–3702 (1973).
14. A.O. Rodin: Grain Boundary Diffusion in High-Purity Al. Effect of Concurrent Cu Segregation. Ph.D. Thesis, Moscow Steel and Alloys Institute, 1999.
15. M.S. Daw and M.I. Baskes: Embedded-atom method—Derivation and application to impurities, surfaces, and other defects in metals. *Phys. Rev. B* **29,** 6443 (1984).
16. S.M. Foiles, M.I. Baskes, and M.S. Daw: Embedded-atom-method functions for the fcc metals Cu, Ag, Au, Ni, Pd, Pt, and their alloys. *Phys. Rev. B* **33,** 7983 (1986).
17. G.J. Ackland and V. Vitek: Many-body potentials and atomic-scale relaxations in noble-metal alloys. *Phys. Rev. B* **41,** 10324 (1990).
18. M.W. Finnis and J.E. Sinclair: A simple empirical n-body potential for transition-metals. *Philos. Mag. A* **50,** 45 (1984).
19. M.I. Mendelev, S. Han, D.J. Srolovitz, G.J. Ackland, D.Y. Sun, and M. Asta: Development of new interatomic potentials appropriate for crystalline and liquid iron. *Philos. Mag. A* **83,** 3977 (2003).
20. A. Il'inskii, S. Slyusarenko, O. Slukhovskii, I. Kaban, and W. Hoyer: Structure of liquid Fe-Al alloys. *Mater. Sci. Eng. A* **325,** 98 (2002).
21. K. Sorensen and G. Trumpy: Dynamical properties of Fe 57 dissolved in Al observed by Mossbauer-effect. *Phys. Rev. B* **7,** 1791 (1973).
22. W.B. Alexander and L.M. Slifkin: Diffusion of solutes in aluminum and dilute aluminum alloys. *Phys. Rev. B* **1,** 3274 (1970).
23. G. Rummel, T. Zumkley, M. Eggersmann, K. Freitag, and H. Mehrer: Diffusion of implanted 3d-transition elements in aluminum.1. Temperature-dependence. *Z. Metallkde* **86,** 122 (1995).
24. M.I. Mendelev, R. Krishnamurthy, D.J. Srolovitz, A.O. Rodin, and B.S. Bokstein: (unpublished).
25. S.M. Foiles: Calculation of the surface segregation of Ni-Cu alloys with the use of the embedded-atom method. *Phys. Rev. B* **32,** 7685 (1985).

APPENDIX I. The interatomic potentials for Al-Fe alloys.

Function	Value	Cutoffs
$\varphi^{AlAl}(r)$	$(2433.5591473227/r)[0.1818\exp(-22.713109144730r) + 0.5099\exp(-6.6883008584622r)$	0–1.6
	$+ 0.2802\exp(-2.8597223982536r) + 0.02817\exp(-1.4309258761180r)]$	
	$+ \exp(6.0801330531321 - 2.3092752322555r + 0.042696494305190r^2 - 0.07952189194038r^3)$	1.6–2.25
	$+ 17.222548257633\ (3.2 - r)^4$	2.25–3.2
	$- 13.838795389103\ (3.2 - r)^5$	2.25–3.2
	$+ 26.724085544227\ (3.2 - r)^6$	2.25–3.2
	$- 4.8730831082596\ (3.2 - r)^7$	2.25–3.2
	$+ 0.26111775221382\ (3.2 - r)^8$	2.25–3.2
	$- 1.8864362756631\ (4.8 - r)^4$	2.25–4.8
	$+ 2.4323070821980\ (4.8 - r)^5$	2.25–4.8
	$- 4.0022263154653\ (4.8 - r)^6$	2.25–4.8
	$+ 1.3937173764119\ (4.8 - r)^7$	2.25–4.8
	$- 0.31993486318965\ (4.8 - r)^8$	2.25–4.8
	$+ 0.30601966016455\ (6.5 - r)^4$	2.25–6.5
	$- 0.63945082587403\ (6.5 - r)^5$	2.25–6.5
	$+ 0.54057725028875\ (6.5 - r)^6$	2.25–6.5
	$- 0.21210673993915\ (6.5 - r)^7$	2.25–6.5
	$+ 0.032014318882870\ (6.5 - r)^8$	2.25–6.5
$\varphi^{AlFe}(r)$	$(4867.1182946454/r)[0.1818\exp(-25.834107666296r) + 0.5099$	
	$\exp(-7.6073373918597r) + 0.2802\exp(-3.2526756183596r)$	
	$+ 0.02817\exp(-1.6275487829767r)]$	0–1.2
	$+\exp(6.6167846784367 - 1.5208197629514r - 0.73055022396300r^2$	1.2–2.2
	$- 0.038792724942647r^3)$	
	$- 4.1487019439249\ (3.2 - r)^4$	2.2–3.2
	$+ 5.6697481153271\ (3.2 - r)^5$	2.2–3.2
	$- 1.7835153896441\ (3.2 - r)^6$	2.2–3.2
	$- 3.3886912738827\ (3.2 - r)^7$	2.2–3.2
	$+ 1.9720627768230\ (3.2 - r)^8$	2.2–3.2
	$+ 0.094200713038410\ (6.2 - r)^4$	2.2–6.2
	$- 0.16163849208165\ (6.2 - r)^5$	2.2–6.2
	$+ 0.10154590006100\ (6.2 - r)^6$	2.2–6.2
	$- 0.027624717063181\ (6.2 - r)^7$	2.2–6.2
	$+ 0.0027505576632627\ (6.2 - r)^8$	2.2–6.2

(continued)

APPENDIX I. The interatomic potentials for Al-Fe alloys. (Continued)

Function	Value	Cutoffs
$\varphi^{FeFe}(r)$	$(9734.2365892908/r)[0.1818\exp(-28.616724320005r) + 0.5099\exp(-8.4267310396064r)$	
	$+ 0.2802\exp(-3.6030244464156r)$	
	$+ 0.02817\exp(-1.8028536321603r)]$	0–1.0
	$+ \exp(7.4122709384068 - 0.64180690713367r - 2.6043547961722r^2$	1.0–2.05
	$+ 0.62625393931230r^3)$	
	$- 27.444805994228\ (2.2 - r)^3$	2.05–2.2
	$+ 15.738054058489\ (2.3 - r)^3$	2.05–2.3
	$+ 2.2077118733936\ (2.4 - r)^3$	2.05–2.4
	$- 2.4989799053251\ (2.5 - r)^3$	2.05–2.5
	$+ 4.2099676494795\ (2.6 - r)^3$	2.05–2.6
	$-0.77361294129713\ (2.7 - r)^3$	2.05–2.7
	$+ 0.80656414937789\ (2.8 - r)^3$	2.05–2.8
	$- 2.3194358924605E + 00\ (3.0 - r)^3$	2.05–3.0
	$+ 2.6577406128280\ (3.3 - r)^3$	2.05–3.3
	$- 1.0260416933564\ (3.7 - r)^3$	2.05–3.7
	$+ 0.35018615891957\ (4.2 - r)^3$	2.05–4.2
	$- 0.058531821042271\ (4.7 - r)^3$	2.05–4.7
	$- 0.0030458824556234E\ (5.3 - r)^3$	2.05–5.3
$\Psi^{AlAl}(r)$	$0.00019850823042883\ (2.5 - r)^4$	0–2.5
	$+ 0.10046665347629\ (2.6 - r)^4$	0–2.6
	$+ 1.0054338881951E\text{-}01\ (2.7 - r)^4$	0–2.7
	$+ 0.099104582963213\ (2.8 - r)^4$	0–2.8
	$+ 0.090086286376778\ (3.0 - r)^4$	0–3.0
	$+ 0.0073022698419468\ (3.4 - r)^4$	0–3.4
	$+ 0.014583614223199\ (4.2 - r)^4$	0–4.2
	$- 0.0010327381407070\ (4.8 - r)^4$	0–4.8
	$+ 0.0073219994475288\ (5.6 - r)^4$	0–5.6
	$+ 0.0095726042919017\ (6.5 - r)^4$	0–6.5
$\Psi^{AlFe}(r)$	$0.010015421408039\ (2.4 - r)^4$	0–2.4
	$+0.0098878643929526\ (2.5 - r)^4$	0–2.5
	$+ 0.0098070326434207\ (2.6 - r)^4$	0–2.6
	$+ 0.008.4594444746494\ (2.8 - r)^4$	0–2.8
	$+ 0.0038057610928282\ (3.1 - r)^4$	0–3.1
	$- 0.0014091094540309\ (5.0 - r)^4$	0–5.0
	$+ 0.0074410802804324\ (6.2 - r)^4$	0–6.2
$\Psi^{FeFe}(r)$	$11.686859407970\ (2.4 - r)^3$	0–2.4
	$- 0.014710740098830\ (3.2 - r)^3$	0–3.2
	$+ 0.47193527075943\ (4.2 - r)^3$	0–4.2
$\Phi^{Al}(\rho)$	$-\rho^{1/2} + 0.000093283590195398\rho^2 - 0.0023491751192724\rho\ln\rho$	
$\Phi^{Fe}(\rho)$	$-\rho^{1/2} - 0.00067314115586063\rho^2 + 0.000000076514905604792\rho^4$	